Effects of boundary conditions on coherent synchrotron radiation in echo-enabled harmonic generation

Dmitrii Samoilenko,[1,2,*] Demin Zhou,[3,†] Najmeh Mirian,[4] Wolfgang Hillert,[1] and Pardis Niknejadi[2]

[1]*Universität Hamburg, Institute of Experimental Physics, Luruper Chaussee 149, 22761, Hamburg, Germany*
[2]*Deutsches Elektronen-Synchrotron DESY, Notkestrasse 85, 22607, Hamburg, Germany*
[3]*High Energy Accelerator Research Organization (KEK), 1-1 Oho, Tsukuba, 305-0801, Ibaraki, Japan*
[4]*Helmholtz-Zentrum Dresden-Rossendorf HZDR, Bautzner Landstrasse 400, 01328, Dresden, Germany*

(Received 16 April 2024; accepted 26 March 2025; published 23 April 2025)

Coherent synchrotron radiation (CSR) is known for its detrimental effects on the performance of free electron lasers (FEL). While it is commonly considered a source of beam quality degradation in linacs, in externally seeded FEL schemes, CSR is known to spoil the bandwidth of the FEL radiation. Investigating CSR's effect on seeded FELs requires a realistic estimation of CSR-induced energy modulations, known as wakes. Several models exist for calculating CSR wakes, differing in their treatment of transient and shielding effects. This work applies various models to compute CSR wakes in a magnetic chicane. In particular, it highlights the importance of the chicane chamber shielding for relatively long electron bunches used in seeded FELs. We use the practical example of the echo-enabled harmonic generation (EEHG) seeding technique to establish that proper consideration of transient and shielding effects is essential for estimating the impact of CSR on seeded FEL performance. This corrected estimate is vital for reaching the near-Fourier limit bandwidth of EEHG by the currently available methods.

DOI: 10.1103/PhysRevAccelBeams.28.040702

I. INTRODUCTION

Electrons traversing through a bending magnet undergo radiative interactions across a broad spectral range. At wavelengths comparable to or longer than the electron bunch length, this interaction manifests itself coherently and is known as coherent synchrotron radiation (CSR). Generally speaking, CSR has a detrimental effect on the performance of free electron lasers (FELs) by increasing the energy spread and emittance [1,2] and amplifying the microbunching instability [3,4] of the electron beams in the linac, particularly in bunch compressors. Within advanced seeded FEL schemes [5,6], CSR can significantly contribute to spectral broadening and wavelength shift of output radiation [7–10]. Since a primary objective of seeding methods is to produce near-Fourier-limited bandwidth pulses, these CSR-induced effects are undesirable and crucial to understand. Existing research on seeded FELs focuses primarily on mitigating the impact of CSR-induced energy modulation, known as CSR wake, by employing simplified models for CSR effects. Predominately used 1D models of CSR [11,12] have revealed that transient effects at the entrance and exit of short bending magnets of dispersive chicanes can contribute considerably to CSR effects. Further refinements consider the shielding effect of parallel plates [13–15] and the interference between consecutively aligned bending magnets [16,17]. To date, most studies on CSR with chamber shielding for FELs have utilized the image charge method within approaches based on either the Liénard-Wiechert potential or Jefimenko's formulation of Maxwell's equations (for a comparison of these two approaches, see [14]). Meanwhile, for electron storage rings, solving the parabolic equations in the frequency domain for fields with boundary conditions has been extensively investigated [12,18–22]. In [23], it was demonstrated that the instantaneous impedance [24], calculated using this frequency-domain method, can effectively describe the impact of CSR effects in a linac. This parametrization of CSR effects, initially developed for electron storage rings, simultaneously considers transient effects, interference along the beam line, and shielding of a transversely closed chamber. In this paper, we build upon the foundational work presented in [23], delving into a comprehensive examination of various 1D CSR models. Reported experimental explorations [25,26] suggest that 1D approximations align closely with experimental data for

*Contact author: dmitrii.samoilenko@desy.de
†Contact author: dmzhou@post.kek.jp

our discussion, and thus the extension to 2D and 3D models has not been pursued at this time. Our primary focus lies on assessing their impacts within the context of advanced seeded FEL schemes and optimization of such schemes in the case of linearly chirped electron beams. For further discussions on 2D and 3D models for CSR, the reader is referred to [25,27–29] and the references therein. In particular, Talman's extension of the time-domain approach to a line charge addresses some limitations of classical electrodynamics and provides a comprehensive overview of parameters critical for machine design. More recently, Mayes presented a detailed review of the three primary types of CSR models in [29], offering valuable insights into their applications and limitations. Our work addresses a consequential gap in the study of CSR effects by highlighting the significance of bunching bandwidth as a more direct and relevant measure for evaluating the performance of seeded FELs. While Ref. [8] does use bunching bandwidth as a measure to mitigate CSR effects, it does not, however, account for chamber effects. On the other hand, other notable studies mentioned above use metrics such as emittance [15,25], energy spread [17], and beam longitudinal phase space [13], which are indeed suitable to specific machine designs but do not directly translate to the case for seeded FEL performance.

Building on these distinctions, we structure our investigation to systematically address the effects of boundary conditions of CSR and their implications for seeded FELs. The structure of our investigation is organized as follows: Section II outlines different 1D CSR models, setting the stage for a nuanced understanding of their implications. Section III provides the theoretical foundation necessary for quantifying the influence of energy modulation on the echo-enabled harmonic generation (EEHG) seeded FEL scheme. This section also introduces a specific case study—the first seeding chicane at the upgraded FLASH facility [30]—illustrating the practical application of the theoretical concepts presented. The result and analysis in Sec. IV features impedance calculations with CSRZ [23] and particle tracking simulations with ELEGANT [31]. Finally, Sec. V concludes the paper by summarizing our key findings and outlining future research directions.

II. THEORY: 1D MODELS FOR CSR

The 1D approximation is widely adopted in models calculating CSR effects. This approximation simplifies the analysis by projecting the electron beam's transverse distribution onto the beam trajectory axis. Therefore, the charge distribution is represented by the line charge density $\lambda(s,z)$, where s is the position of the center of the bunch along the reference beam orbit and z is the relative position inside the bunch. The scope of validity and potential importance of this approximation is discussed fully, e.g., in Refs. [25,28]. To determine the validity of the 1D approximation, one can evaluate the criterion from [1]:

$$\sigma_\perp \sigma_z^{-2/3} R^{-1/3} \ll 1, \tag{1}$$

where $\sigma_\perp$ is the transverse beam size, σ_z is the bunch length, and R is the bending radius. We can categorize CSR models based on (i) the inclusion of transient effects and (ii) boundary conditions. The transient effects describe the CSR interaction between parts of the electron bunch when the bunch enters or leaves the bend. The boundary conditions allow for considering the CSR shielding by the conductive walls of the chicane chamber.

A. Steady-state 1D CSR models

The most basic model is the steady-state model in free space (FS-SS). The formulation of CSR impedance of a bend in this case can be found in Refs. [32,33].

A more advanced model is the steady-state parallel plates (PP) model. Here, we assume that the beam is located in the middle between two perfectly conducting infinite parallel plates. The CSR impedance for this model is given in [19] and determines a shielding threshold of $k_{\mathrm{th}} = \pi\sqrt{R/a^3}$, where a is the distance between the plates (i.e., chamber height). Below this threshold wave number, the CSR fields are strongly suppressed. The CSR effects can be negligible for bunches with length $\sigma_z \gg 1/k_{\mathrm{th}}$ if no microbunching occurs within the bunch. On the other hand, when $\sigma_z \ll 1/k_{\mathrm{th}}$, CSR effects are dominated by high-frequency CSR impedances that are not influenced by the boundary surfaces. In this case, free-space CSR models are applicable for simulations. Our exploration indicates that this model exhibits limitations when applied to systems experiencing notable compression in short magnets, as in our EEHG-FLASH scenario and, by extension, similar setups.

B. Free-space 1D CSR model with transient effects

The free-space model with transient effects (FS-TR) is the native CSR model for ELEGANT code. The implementation of this model is discussed in detail in [34], where the CSR wakefunction follows [11]. The formulation of this model in terms of the CSR impedance in the frequency domain is discussed in [23].

The longitudinal wake function of a bunch $W_\parallel(s,z)$ is represented by the sum of two terms, which represent the steady-state CSR component and the entrance transient part.

In this model, the instantaneous CSR wake felt by the beam at distance s from the bend entrance depends only on the local bunch profile at s, not the bunch profile at $s' < s$. The slippage effects are modeled by introducing a characteristic slippage length. The instantaneous CSR wake function and the corresponding impedance of the bend can be found in [23].

The wakes created inside the dipole can be transported through a drift using CSRDRIFT [35] element in ELEGANT. In this case, the postdipole CSR wakes are calculated

following [36]. The corresponding point-charge wake function and impedance cannot be analytically formulated.

In practical calculations using ELEGANT, the electron distribution is projected on the s axis and smoothed to facilitate the numerical calculation. The bend and the downstream drift are sliced, and the wakes are calculated for each slice and applied to the electron bunch with a local longitudinal profile before it enters the next slice.

C. 1D CSR model using CSRZ code

CSRZ calculates the electromagnetic fields along the beamline by solving Maxwell's equations with the paraxial approximation [19]. The beam line is characterized by s-dependent bending radius $R(s)$ along the beam orbit and a totally reflecting rectangular chamber of a fixed shape. In the case of the chicane depicted in Fig. 2, $R^{-1}(s)$ is a step function equal to $\pm R^{-1}$ in a bend and 0 in a drift. The transverse charge density is assumed to have a 2D Gaussian distribution and to not vary along s in the CSRZ code. The longitudinal component of the electric field gives the longitudinal instantaneous impedance. For more details on the formulation of the model and its implementation see [21] In practical calculations, the beam line is sliced into a certain number of sections. For each section, the impedance is lumped by integrating the instantaneous impedance between positions s_1 and s_2. The integrated impedance of each section is then imported into the ELEGANT tracking simulation using the ZLONGIT [35] element located at s_2.

In our case, the impedance is calculated stepwise for the whole chicane, allowing CSR fields to propagate into the drifts and subsequent dipoles.

Slicing the beam line into a large number of sections can be computationally expensive. Nevertheless, using sufficient slicing is important when the line charge distribution $\lambda(s,z)$ changes significantly along s. This is the case, for example, inside a chicane if the electron beam has a strong linear chirp. In this work, we assume a nominal chirp value of 15 MeV/ps (or $h = 0.016$ if we follow the notation in [37]). For our case, it proved to be sufficient to slice each dipole in four parts and each drift in two parts (see Appendix A).

This method can be extended to study 2D and 3D CSR effects to some extent, since the fields and impedance can be computed as functions of s and the transverse coordinates. The space-dependent impedance can be used to construct the corresponding wake functions, which can then be applied to calculate the wake force by convolution with the beam distribution, as demonstrated in [38]. This approach is at least applicable in cases where the beam is not strongly energy chirped. However, if the beam distribution evolves rapidly along the beam line, for instance due to a large energy chirp resulting in a larger transverse size, the usual expression for the wakefields, based on the rigid-beam approximation, needs to be modified (see [39] for a relevant discussion).

Another approach is to solve the problem with the shielding of circular, elliptical, or even arbitrarily shaped chambers. Efforts have been made in this direction (see, for example, [18,40–42]), but further research is needed to address cases where chamber shielding has strong impacts on beam dynamics or CSR field dynamics.

III. EFFECT OF CSR WAKES ON EEHG

The theories for the EEHG scheme have been well established in the literature. In this section, we compile the necessary formulations for completeness and to facilitate discussions. The equations governing the phase space evolution of the beam in the EEHG scheme are formulated as per [43]:

$$\begin{aligned} P_1 &= P + A_1(z)\sin(k_1 z) + \Delta p_1(z) \\ z_1 &= z + B_1 P_1/k_1 \\ P_2 &= P_1 + A_2(z_1)\sin(k_2 z_1) + \Delta p_2(z_1) \\ z_2 &= z_1 + B_2 P_2/k_2, \end{aligned} \tag{2}$$

where $P = (E - E_0)/\sigma_E$ is the normalized energy deviation from the central energy E_0, $A_{1,2}(z) = \Delta E_{1,2}(z)/\sigma_E$ is the normalized energy modulation induced in the first and the second modulator, respectively, $k_{1,2}$ is the wave number of the first and the second seed laser, respectively, $B_{1,2} = k_{1,2} R_{56}^{(1,2)} \sigma_e/E$ is the normalized dispersion in the first and the second chicane, respectively, E is the energy and σ_E is the initial uncorrelated energy spread. Δp_1 represents energy distortions upstream of the first chicane, e.g., electron beam energy chirp induced in the linac. The effect of pure linear chirp on the spectral properties of EEHG was reported in [37]. It was demonstrated that linear chirp induces a slight wavelength shift of the resulting harmonic, but the efficiency of the harmonic conversion can be easily recovered by adjusting $R_{56}^{(2)}$.Δp_2 represents any energy distortion taking place upstream of the second chicane.

To investigate the effect of Δp_2 on the EEHG efficiency, we can use the Fourier series to represent Δp_2 as a superposition of monochromatic modulations of different amplitudes [43,44]:

$$\Delta p_2 = \sum_{\mu=0}^{\infty} p_2(k_\mu)\sin(k_\mu z + \phi_{2\mu}), \tag{3}$$

where $\phi_{2\mu}$ is a random phase. The efficiency of the harmonic conversion is described by the bunching factor at the target wavelength. In the absence of Δp_2, for ideal electron beam distribution, the bunching factor is [6]:

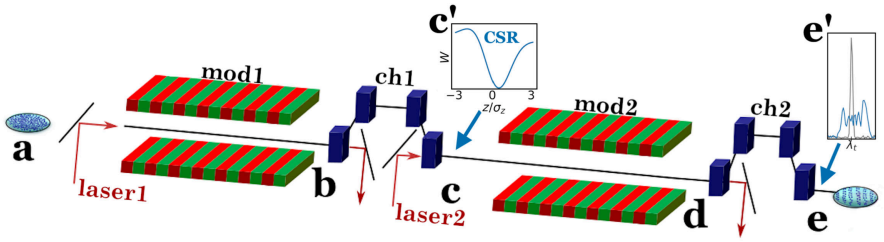

FIG. 1. Typical layout of EEHG seeding scheme: a smooth Gaussian bunch at a obtains a sinusoidal energy modulation at b. The modulation is oversheared by the first chicane at c, where the bunch obtains CSR-induced wake illustrated in c'. Another sinusoidal energy modulation is induced by the laser at d. The bunching is created by the second chicane at e, where the bunching spectrum is affected by CSR, as illustrated in e'.

$$\bar{b}_{nm}(k_E) = e^{-\xi_E^2/2} J_n(-\xi_E A_1) J_m(-a_E A_2 B_2), \tag{4}$$

where $a_E = n + mk_2/k_1$ is the harmonic number, $k_E = a_e k_1$ is the corresponding wave number, n and m are integer numbers, and $\xi_E = nB_1 + a_E B_2$ is the EEHG scaling factor. This factor is known to help characterize the EEHG performance and is optimized approximately at $\xi_E = j'_{n,1}/A_1$ where $j'_{n,1}$ is the first root of J'_n.

If the energy distortion Δp_2 and second laser A_2 are sufficiently slowly varying longitudinally that we can approximate their functional dependence as $z_1 \approx z$, then combining Eqs. (2) and (3), the bunching at the harmonic peak becomes [43]:

$$b_{nm}(k_E) = \bar{b}_{nm}(k_E) \times \prod_{\mu=0}^{\infty} \sum_{l_1=-\infty}^{\infty} (-1)^{l_1} J_{l_1}[-a_E B_2 p_2(k_\mu)] e^{-il_1\varphi_{2\mu}}. \tag{5}$$

From the above equation, we can deduce the effect of energy distortion Δp_2 on the EEHG bunching spectrum by different monochromatic modulation amplitudes p_2. In particular, the corrected bandwidth is given by

$$\sigma_k^2 = \bar{\sigma}_k^2 + \sum_{\mu=0}^{\infty} \left[\frac{(a_E B_2)^2}{2} (p_2(k_\mu) k_\mu)^2 \right], \tag{6}$$

where $\bar{\sigma}_k$ is the bandwidth for $\Delta p_2 = 0$.

In this work, the parameter Δp_2 is the energy modulation induced by the CSR inside the first chicane. It is expressed in terms of the wake potential $W_\parallel$ discussed in Sec. II

$$\Delta p_2 = \frac{qW_\parallel}{\sigma_E}. \tag{7}$$

Therefore, after presenting the example case of FLASH, we continue with the results from different models of CSR and compare the CSR effect on EEHG performance in each case.

A. Example case: EEHG chicane at FLASH

As a practical exploration, we consider the 4 nm EEHG operation mode at the FLASH facility at DESY, which is expected to be operational in the second half of 2025 [45]. A schematic depiction of the EEHG setup is presented in Fig. 1.

The first modulator couples the first seed laser with a wavelength of 300 nm to the electron beam and induces a coherent sinusoidal energy modulation in the electron beam. The first chicane overshears the induced modulation and creates horizontal stripes in the longitudinal phase space. The second modulator imprints another coherent sinusoidal modulation at the same wavelength, and finally, the second chicane is used to shear the new modulation and create the final bunching structure. Strong longitudinal dispersion is required to realize the essential overshearing in the first chicane, which can be achieved using relatively large bending angles. This typically enhances the radiative forces [11]. Therefore, this study focuses on CSR wakes obtained by the electron bunch in the first chicane, where the effects of CSR are expected to be notably prominent. However, the result could be relevant to any scheme with a highly dispersive segment.

Figure 2 shows the layout of the first chicane in FLASH and indicates its geometric parameters.

The segments of interest from the beam line can be described by (B1, D1, B2, D2, B3, D1, B4) where "B" denotes a bend and "D" denotes a drift. According to the chicane configuration, B2 = B3 = −B1 and B4 = B1. The design values of these beam line components are given in Table I.

The full height of the chamber along the chicane is 10 mm. The width of the chamber varies along the beam

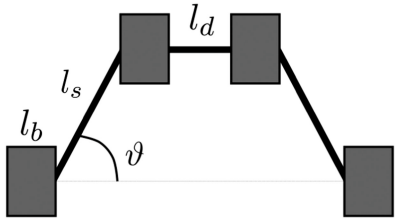

FIG. 2. Layout of ch1. The values of geometric parameters are given in Table I.

TABLE I. Geometrical parameters of ch1. Definition of the measures is shown in Fig. 2.

l_b	0.42 m
l_s	2 m
l_d	0.444 m
ϑ	2.24°
R_{56}	7.05 mm
Chamber inner sizes	10 mm × 20 mm

line. For impedance calculations using the CSRZ code, we choose a fixed width of 20 mm since the code only accepts a frozen chamber cross section. Table II specifies the most relevant beam parameters for simulations.

Since we are investigating model-dependent CSR effects, we simplify the choices of beam parameters with reasonable assumptions. At the entrance of the seeding section, the beam current profile is assumed to be perfect Gaussian; that is, the microbunching from the upstream linac is neglected. The electron beam energy chirp at the entrance is neglected for the discussion in Sec. IV A. The seed laser pulses are assumed to be infinitely long, i.e., the whole electron bunch is evenly seeded. Laser-induced energy modulation at 300 nm has been seen to have no effect on the long-wavelength CSR wake. These assumptions enable us to isolate the influence of long-wavelength CSR wake on EEHG bunching from other factors, facilitating a deeper understanding of its underlying mechanism. It is worth noting that a unique feature of the CSRZ simulation setup used in the above model comparisons is its seamless integration into multistage start-to-end simulation workflows. This approach ensures that the computationally intensive wakefield calculations are aligned with the frequencies of interest for start-to-end simulations. For instance, beams modeled with space charge effects in the linac and compression sections upstream exhibit micron-level bunching in their current profiles and beam centroid displacements along the longitudinal axis of the beam. In such setups, provided the beam energy and path through the chicane remain consistent, different beams from the upstream section of the chicane described in the table can be used. Also, the downstream sections can be optimized by varying the second seed laser pulse properties, dispersion in the bunching chicane, and radiator taper profiles to achieve specific working points. Longer or chirped seed laser pulses may help mitigate or counteract the effects of chirp and CSR but inherently possess broader bandwidths, making optimizing a working point dependent on high precision control of parameters and user-defined objectives. An extended study on these start-to-end workflows is planned for the future. The working point for the study presented here was selected based on EEHG optimization and a modified Ming Xie curve [46,47] that accounts for the unique characteristics of seeded pre-bunched beams (see Appendix D for details on the modified Ming Xie criteria for EEHG setup). This approach significantly reduces the parameter space and the number of scans for optimization [48].

TABLE II. Simulation parameters. E-beam is electron beam.

Initial E-beam parameters	
Central energy	1350 MeV
Slice energy spread	150 keV
Bunch length rms (σ_z)	96 μm
Peak current	500 A
Normalized emittance	0.6 mm · mrad
Seeding section parameters	
Seed lasers wavelength	300 nm
A_1	3.10
$R_{56}^{(1)}$	7.05 mm
A_2	5.18
$R_{56}^{(2)}$	81.25 μm

IV. SIMULATION RESULTS

A. Comparison of 1D CSR models

To verify the validity of the 1D approximation in our case, we evaluated Eq. (1) for the given FLASH parameters (see Tables I and II). The evaluation yields $\sigma_\perp \sigma_z^{-2/3} R^{-1/3} \approx 0.01 \ll 1$, which justifies the use of 1D models. To examine the transient effects and chamber shielding, we compare the impedance and corresponding wakes of the aforementioned 1D CSR models for the first seeding chicane of FLASH.

The total CSR impedance and wakes of one bend are compared in Figs. 3 and 4. The maximum wave number is chosen to be 50 mm^{-1}, which is about $5/\sigma_z$. We expect

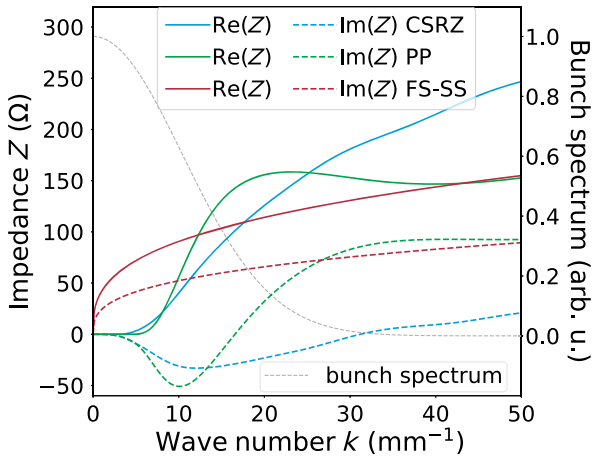

FIG. 3. Total impedance of one bend with $R = 10.7$ m and $l_b = 0.42$ m. Each pair of solid and dashed lines with the same color indicates the real and imaginary impedances by a specific model. The dashed gray line indicates the spectrum of a Gaussian bunch with $\sigma_z = 96$ μm.

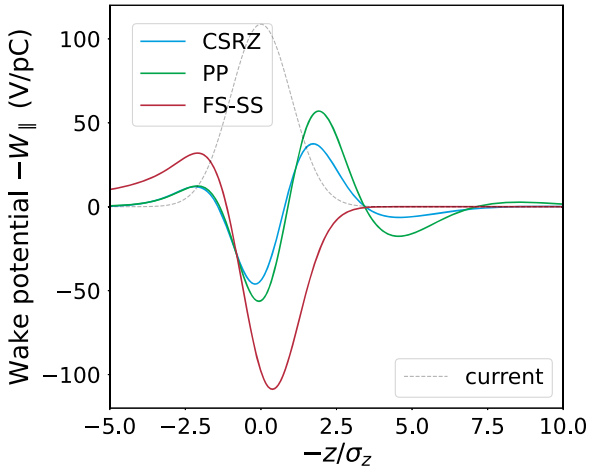

FIG. 4. Total wake potential of one bend for a Gaussian bunch with $\sigma_z = 96$ μm, calculated from the impedances of Fig. 3. The bunch head is to the left.

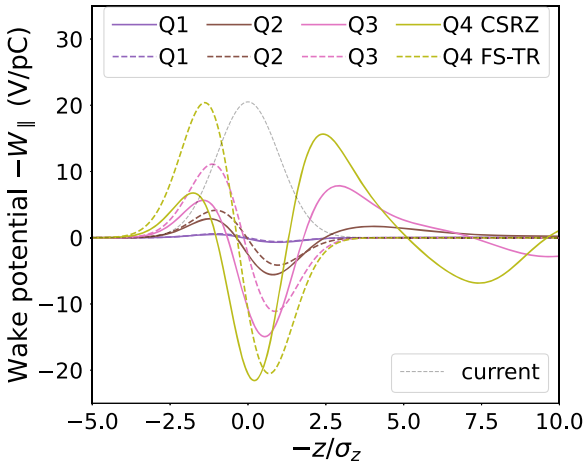

FIG. 5. CSR wakefield per quarter at the first bend (B1) of ch1 for a Gaussian bunch with $\sigma_z = 96$ μm. The symbol Q*i* indicates the *i*th quarter of the bend. The solid and dashed lines are given by the CSRZ code and FS-TR model of [34], respectively.

such spectral coverage to be sufficient to calculate the CSR wake potential. It can be seen that with a bunch length of 96 μm, both chamber shielding and transient effects are important in the chicane. The chamber partially suppresses the overtaking fields felt by the bunch head but also enhances the trailing fields felt by the bunch tail (see Fig. 7 of [14] and Fig. 8 of [16] for similar observations). The underlying physics can be intuitively elucidated using waveguide theory as follows (for a more in-depth exploration of the mathematical aspects of CSR fields within a waveguide, the reader is directed to [22]). Suppose that the electron bunch travels with the speed of light c, the CSR fields of a particle exclusively influence its leading particles and not its trailing ones in free space. However, the existence of metal walls slows the group velocity of the CSR fields, leading them to influence both leading and trailing particles. This reduction in group velocity weakens the tail-to-head CSR fields while enhancing the head-to-tail CSR fields. Figure 4 also shows that the CSRZ and PP models have almost the same amplitude in the head part but differ in the tail part due to the combined effects of the chamber and transients.

Although the wakes calculated by the CSRZ code and the PP model are similar, a s-dependent wake model is preferred for a chicane. This is because the electron bunch length can vary along the beamline, and using an s-dependent model allows for a more accurate representation of the dynamic beam conditions. Figure 5 compares the CSR wakefields in slices of a bend calculated by the CSRZ code and the free-space model with transient effects. The bend is sliced into four pieces. For each slice, the instantaneous impedance is integrated and then used to calculate the local wake potential. In these two models for comparison, transient effects at the entrance are considered. One can see that the chamber shielding is significant for a bunch length of 96 μm in the case of FLASH. For the first quarter, the chamber shielding is not seen and the two models agree well. However, as the fields propagate to the end of the bend, the discrepancy becomes significant.

The CSR emitted at the upstream bend can propagate through a drift and enter the downstream bend. This effect is not considered in the standard 1D model of ELEGANT. The CSRZ code naturally models this interference of CSR between consecutive bends (referred to as multibend interference) by integrating the CSR fields along the entire beamline. For the first chicane of FLASH, we compare the CSR wakefields per quarter bend across three bends (B1, B2, and B3), as shown in Figs. 5–7. The differences in the wakes of B2 and B3 compared to B1 clearly show that the chamber walls guide the CSR fields to propagate along the beamline, primarily affecting the tail of the bunch. Notably,

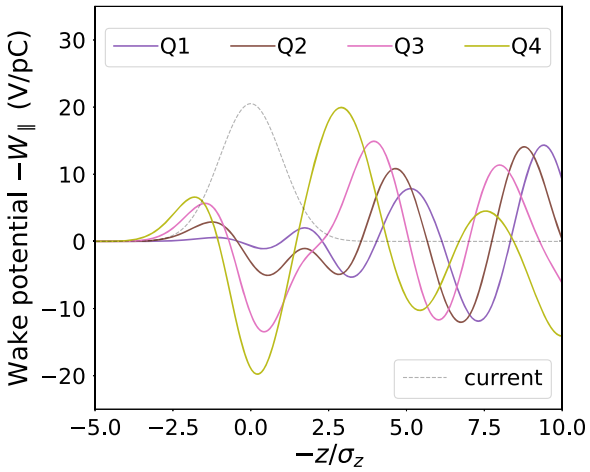

FIG. 6. CSR wakefield per quarter at the second bend (B2) of ch1 for a Gaussian bunch with $\sigma_z = 96$ μm. The symbol Q*i* indicates the *i*th quarter of the bend. The wake potentials are calculated using impedance data from the CSRZ code.

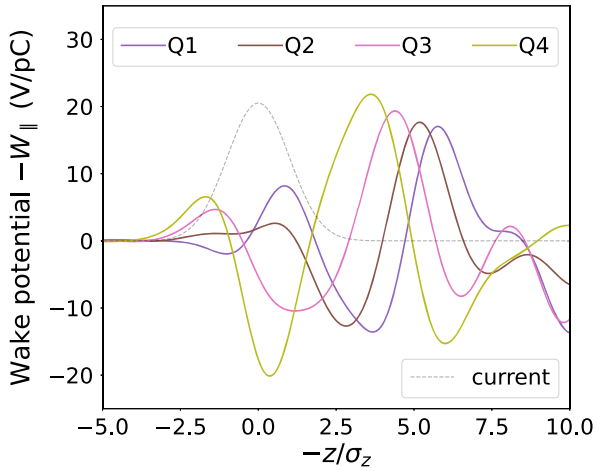

FIG. 7. CSR wakefield per quarter at the third bend (B3) of ch1 for a Gaussian bunch with $\sigma_z = 96$ μm. The symbol Qi indicates the ith quarter of the bend. The wake potentials are calculated using impedance data from the CSRZ code.

the multibend interference significantly modifies the wake strengths in the first quarters of B2 and B3, where transient effects are important. In the fourth quarter, the CSR fields saturate, and the wake strengths align closely with those of the PP-SS model. The multibend interference is observed only relatively far behind the bunch.

The CSR wakefields in the drift following the first bend are compared in Fig. 8. Surprisingly, the discrepancy between CSRZ and the model of [36] is quite large in our case and can only be attributed to the effects of chamber shielding.

So far, we have shown that the boundary conditions can cause the CSR wakefields in the chicane ch1 of EEHG FLASH to differ significantly from those

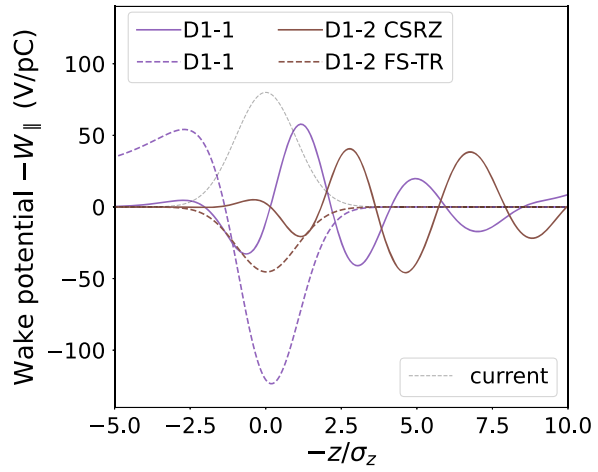

FIG. 8. CSR wakefields in the drift after the first bend for a Gaussian bunch with $\sigma_z = 96$ μm. The symbols D1-1 and D1-2 indicate the first and second 1-m drifts following the first bend. Solid and dashed lines are given by CSRZ and [36], respectively.

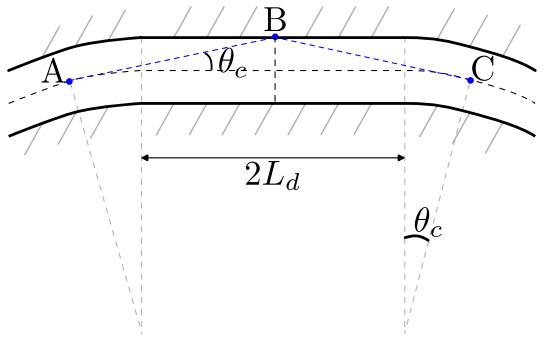

FIG. 9. Ray-tracing illustration of CSR reflected by the outer chamber wall. The CSR is emitted at point A, reflected off the wall at point B, and impacts the beam at point C.

predicted by popular 1D models, with the chosen bunch length of 96 μm. The source of this difference is mainly from the shielding of a closed chamber and the multibend interference.

The transversely closed chamber not only provides shielding but also guides the CSR to trail behind the bunch. If the bunch is short enough, it will not be affected by these trailing fields. This can be further quantitatively illustrated using the ray-tracing analysis demonstrated in [24,49] (see Fig. 6 of [24] and Fig. 3 of [49], along with the relevant discussions therein), considering CSR as ray optics as visualized in [50]. Here, we provide an illustrative example rather than a general theory. Consider two consecutive bends of the same radius R connected by a drift of length $2L_d$ (see Fig. 9), with the distance from the beam orbit to the outer chamber wall assumed to be constant x_o. The CSR field emitted at point A in the upstream bend is reflected at the midpoint B of the drift and reaches point C of the beam orbit in the downstream bend. The catch-up distance, defined as the difference between the paths of the beam orbit and the ray-tracing CSR fields, can be formulated as

$$\Delta s_o = 2R(\tan\theta_c - \theta_c) + 2L_d\left(\frac{1}{\cos\theta_c} - 1\right), \tag{8}$$

with

$$\cos\theta_c = \frac{R(x_o + R) + L_d\sqrt{L_d^2 + 2Rx_o + x_o^2}}{(R + x_o)^2 + L_d^2}. \tag{9}$$

With $L_d = 0$ (i.e., there is no drift between the bends), Eq. (8) reduces to Eq. (16) of [24]. In principle, if the bunch length satisfies $\sigma_z \ll \Delta s_o$, the reflected fields should not be seen by the beam.

Equation (8) can be used to illustrate the CSR fields in the first two quarters of the B2 and B3 bends, as shown in Figs. 6 and 7. For the B2 bend, the CSR fields generated in the previous B1 bend are reflected back to the beam. The parameters are $L_d = l_s/2 = 1$ m, $R = 10.74$ m, and

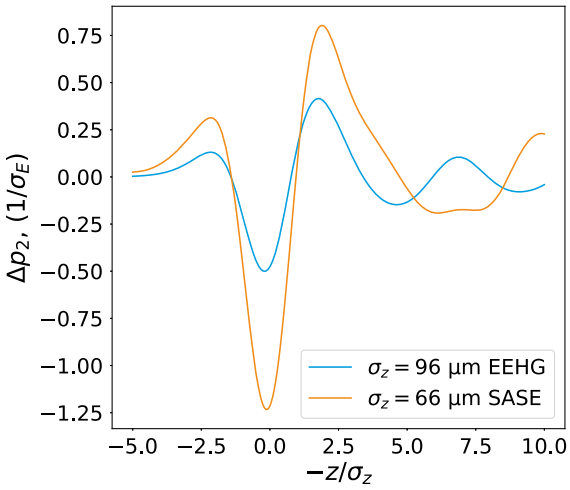

FIG. 10. CSR wakes calculated using CSRZ impedance data for the first chicane in the FLASH EEHG setup and compression chicane for FLASH SASE setup where the bunch lengths are $\sigma_z = 96$ and 66 μm, respectively.

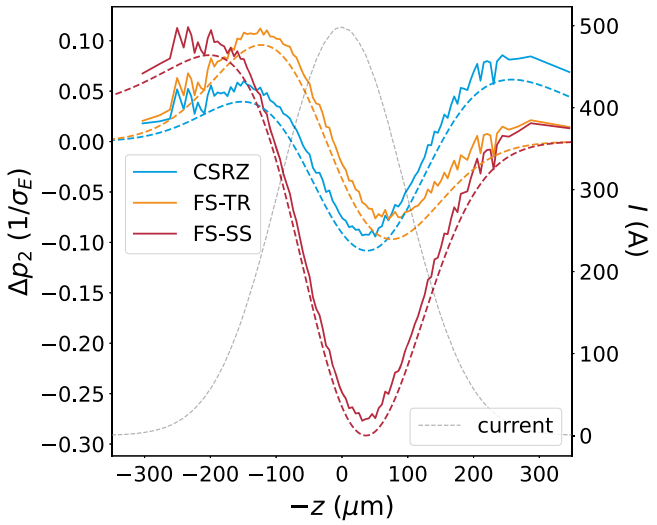

FIG. 11. Energy centroid from particle tracking (solid lines) and theoretical CSR wakes (dashed lines) after the first bend for different CSR models. Bunch current profile is given in black. The bunch head is on the left. Note that the x-axis in this and other plots in Sec. IV B plots is shorter than $\pm 5\sigma_z$ since there are no particles present in the beam distribution's extreme head and tail sections after compression.

$x_0 = 10$ mm, resulting in $\theta_c = 0.54°$ and $\Delta s_o = 0.097$ mm. For the B3 bend, the CSR fields generated in the previous B2 bend are reflected back to the beam. The parameters are $L_d = l_d/2 = 0.222$ m, $R = 10.74$ m, and $x_0 = 10$ mm, resulting in $\theta_c = 1.56°$ and $\Delta s_o = 0.31$ mm. The quantity Δs_o calculated here roughly indicates where the wall reflection modulates the CSR wakefields, and good agreement can be observed between these predictions and Figs. 6 and 7. The quantity θ_c decreases as L_d increases, indicating that the amount of CSR fields reaching the beam orbit in the downstream bend decreases. This is evident by comparing the CSR wakes of the first quarter in B2 and B3.

We also remind the reader that the upper and lower walls, which are parallel to the plane of the beam orbit, modulate the CSR fields in the range of $|z| \sim 1/k_{\mathrm{th}} = 0.097$ mm according to the PP-SS model. This shielding effect, combined with transient effects and out-wall reflection, makes the CSR fields around $|z|/\sigma_z \lesssim 2$ in the first quarter of each bend complex and significantly different from those predicted by the FS-TR model.

The specific dynamics of the EEHG FLASH case present a unique scenario. The bunch length of 96 μm is relatively long compared to Self-Amplified Spontaneous Emission (SASE) FELs. For comparison, the SASE beam line of FLASH features a chicane similar to the one described here. However, while the CSR effect on the beam in the SASE FLASH is more pronounced, see Fig. 10, the shorter bunch might be less affected by the wake.

B. Particle tracking simulations

1. Gaussian bunch

In order to evaluate the effect of CSR on EEHG performance, we start with a simplified case of a non-chirped Gaussian electron bunch. For the first bend, we compare the results of tracking with ELEGANT for CSRZ, FS-TR, and FS-SS models in Fig. 11. As a consistency check, we also add the convolution of a Gaussian bunch with the corresponding impedance to the plots.

The analytically calculated wakes describe the energy centroid from the simulations quite well, since the longitudinal bunch profile does not essentially change inside the first bend. In fact, the same argument can be applied to any point of the chicane, although it is not illustrated in later figures. A notably larger amplitude of Δp_2 for the FS-SS

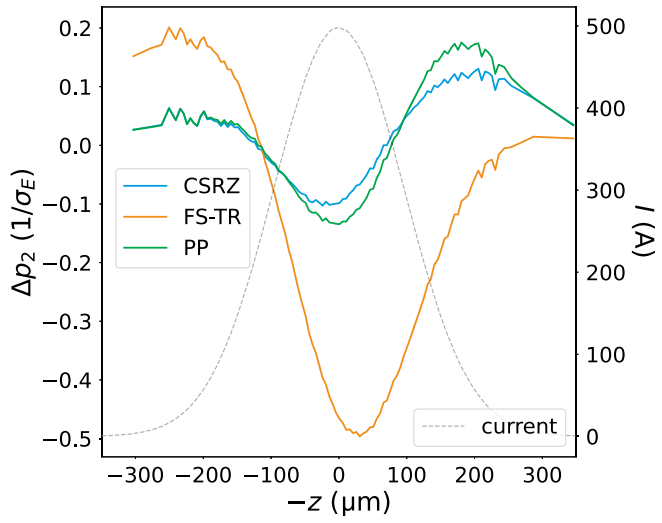

FIG. 12. Energy centroid from particle tracking after the first drift for different CSR models. Bunch current profile is given in black. The bunch head is on the left.

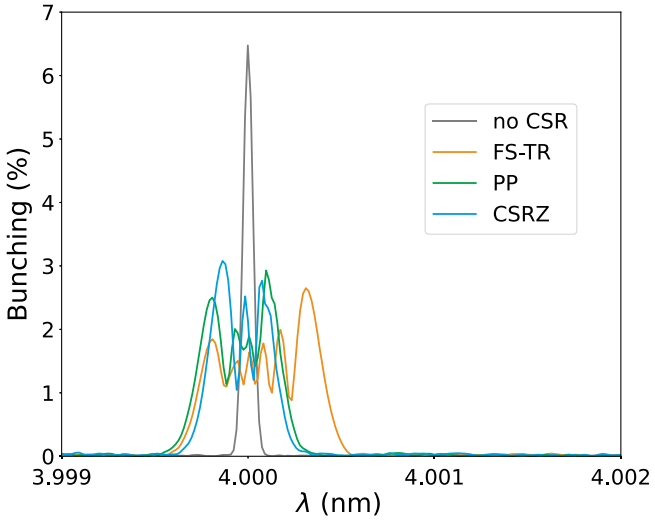

FIG. 13. Bunching spectrum at the exit of ch2 for different CSR models.

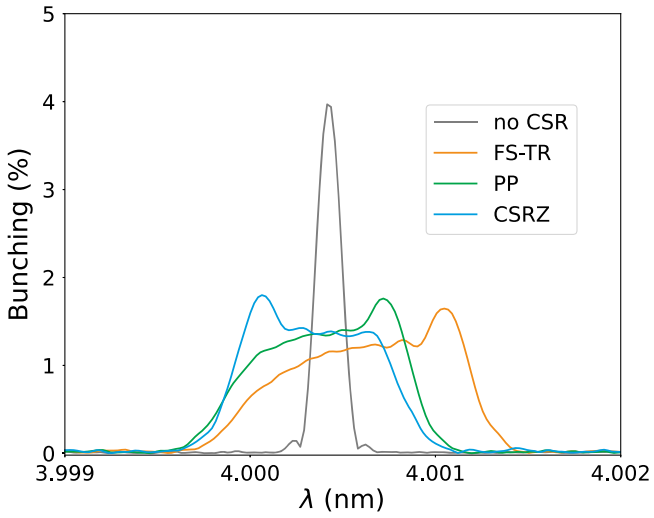

FIG. 14. Bunching spectra for different CSR models with $h = 0.016$ linear chirp. (The mirrorlike similarity in the shapes observed in the spectra is attributed to the sign of the CSR-induced chirp shown in Fig. 12).

model is consistent with Fig. 4 and illustrates the contribution of the transient effects at the bend entrance. Comparing CSRZ to FS-TR reveals suppression of the overtaking field and the energy kick to the tail of the bunch, facilitated by the chamber. Both features are consistent with Fig. 5. Since we have shown that the steady-state FS model is inadequate for our chicane, we are not going to discuss it further. In Fig. 12, we compare the wakes calculated by CSRZ, PP, and FS-TR models in the drift following the bend. We can see that the amplitude of Δp_2 in the FS-TR model is much larger than for the models with shielding, which is consistent with Fig. 8. This is an indication that shielding is essential for the calculation of CSR in FLASH EEHG chicane. The difference between CSRZ and PP-SS models precisely repeats (see Fig. 4).

To quantify the final Δp_2, which enters Eq. (2), we need to track the wakes to the exit of ch1 (given in Appendix B). Based on the calculated CSR wakes at the exit of the chicane, we will determine the effect on the bunching. The EEHG bunching spectrum around 4 nm (shortest harmonic target wavelength) is shown in Fig. 13. CSRZ-based estimation of the bandwidth is (i) ≈20% smaller as compared to PP; (ii) ≈2 times smaller as compared to FS-TR; (iii) still 1 order of magnitude larger as compared to "no CSR." The bandwidths in terms of wavelength for the nonchirped electron beam $\sigma_\lambda(h = 0)$ are given in Table III.

The bandwidth can be also estimated with Eq. (6). For this, we perform a numerical Fourier transform of the CSR wake to extract the spectral components k_μ and their amplitudes $p_2(k_\mu)$. As an example, for the PP model, this results in a bandwidth of $\approx 1.1 \times 10^{-4}$ nm. This value agrees closely with the one provided in Table III. However, the accuracy of the analytical formula does not allow to compare different CSR models. Such modest accuracy is expected, since Eq. (6) is derived in the approximation $k \gg 1/\sigma_z$, which is not fulfilled for the

TABLE III. Comparison of bunching bandwidth for different CSR models with and without electron beam chirp.

Model	$\sigma_\lambda(h = 0)$ (nm)	$\sigma_\lambda(h = 0.016)$ (nm)
No CSR	1.9×10^{-5}	4.4×10^{-5}
FS-TR	2.2×10^{-4}	3.5×10^{-4}
PP	1.5×10^{-4}	2.8×10^{-4}
CSRZ	1.2×10^{-4}	2.6×10^{-4}

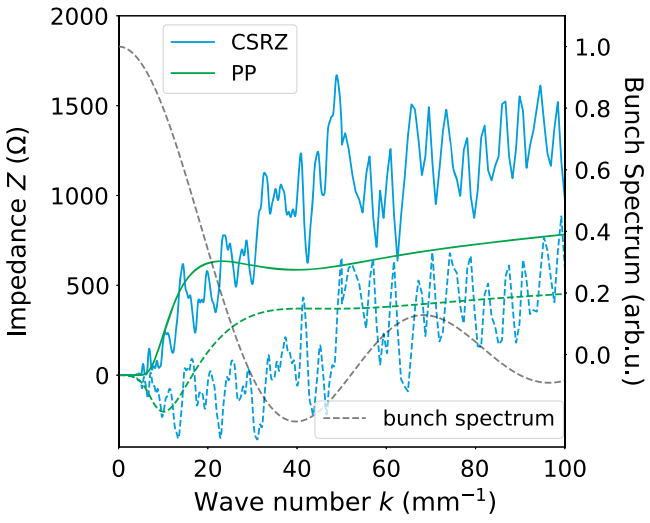

FIG. 15. Impedance of the whole ch1 given by PP and CSRZ models. The spectrum of the rectangular electron bunch is given in gray.

CSR wakes. Nevertheless, the observed agreement indicates that we can attribute the effect of long-wavelength CSR wakes to the same mechanism.

Before discussing the effect of CSR on the bunching spectrum of a chirped electron beam, we need to understand and decouple the effect of the chirp itself. The effect is quantified in Appendix C. In the simulations with chirp, we also compare the bunching spectra for different CSR models, as we did for the nonchirped case.

In Fig. 14, we see that CSR has a more significant effect on the EEHG performance with a strong chirp. The shape of the spectra obtained with each CSR model is very similar to the nonchirped case. Small peaks in Fig. 13 are broadened which is why the spectrum is smooth. The mirrorlike similarity in the shapes observed in the spectra, as shown in Figs. 13 and 14, has been thoroughly investigated—the bandwidth variation results from CSR-induced linear chirp variance along the bunch. In the FS-TR model, the head of the beam has a strong positive chirp, which, coupled with the R_{56} of the second seeding chicane, leads to local decompression of the bunch and manifests as a red shift in the bunching spectrum. In contrast, the CSRZ and PP models result in a symmetrically distributed chirp around the bunch's center, with opposite signs on either side. This distribution correlates with the spectral shapes seen in Fig. 14, which have symmetrical features closer to the central wavelength than the FS-TR's peak. The position of the peaks in CSRZ and PP spectra is then defined by the statistical weights of positive and negative linear chirps within the bunch. The estimated rms bandwidths for the chirped beam $\sigma_\lambda(h = 0.016)$ are given in Table III. The estimated CSR-induced bandwidth is about 2 times larger for the chirped case, which we address to larger CSR wakes in this case, as demonstrated in Fig. 21.

2. Rectangular bunch

While the seeded FEL beamline of FLASH is expected to have a Gaussian current profile, advances in laser pulse shaping for photocathodes may soon enable the generation of more uniform (flattop) current profiles. Such profiles are already achievable in nonsuperconducting machines, though they often introduce second-order chirp as a side effect on the electron beam. Consequently, we extend our study to include these cases here. A rectangular electron bunch is an extreme example of flattop bunches. For this case, we do not repeat the detailed analysis but rather show the change in the final results. The current profile of the rectangular bunch is given by

$$I(z) = \begin{cases} I_0, & |z| < \mathrm{FWHM}/2 \\ 0, & \text{otherwise,} \end{cases} \tag{10}$$

where $\mathrm{FWHM} \approx 2.355 \cdot \sigma_z$ is the full width at half maximum of the Gaussian bunch. In Fig. 15, we show the impedance of the whole ch1 and the spectrum of the rectangular bunch. We see that the spectrum is broader than that of the Gaussian bunch. We also note the spiky structure of the impedance given by the CSRZ model compared to the smoother impedance of the PP model. The spiky impedance spectrum is caused by reflections within the transversely closed chamber, as discussed in Sec. IV A.

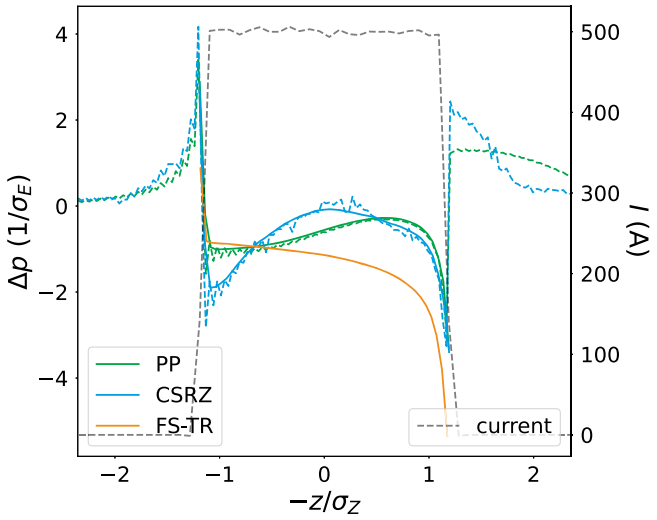

FIG. 16. Energy centroid from particle tracking (solid lines) and theoretical CSR wakes (dashed lines) after ch1 for different CSR models for a rectangular bunch. Bunch current profile is given in black. The bunch head is on the left.

In Fig. 16, we show the CSR wakes after the first EEHG chicane extracted from the particle tracking simulations and compared to analytically calculated wakes as a consistency check. The amplitudes of the wakes are in general

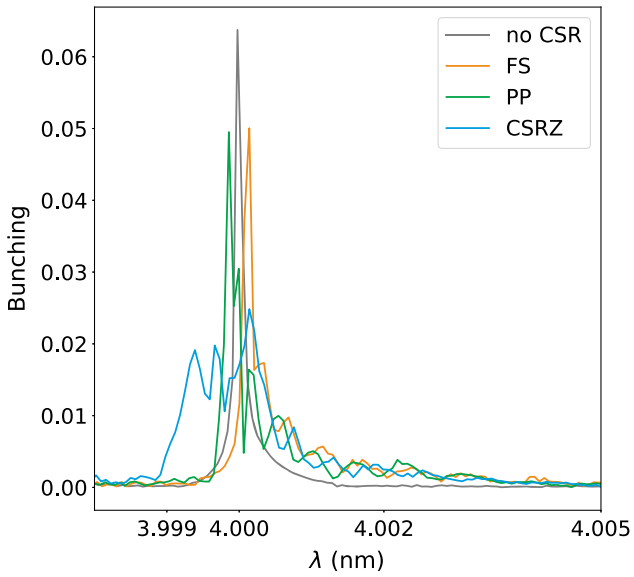

FIG. 17. Bunching spectra for different CSR models for the rectangular bunch.

TABLE IV. rms bandwidths of the bunching spectra for different CSR models of a rectangular electron bunch. If not equal to 0, $h_2 = 1.7 \times 10^{-7}$.

Model	$\sigma_\lambda(h_2 = 0)$ (nm)	$\sigma_\lambda(h_2 \neq 0)$ (nm)
No CSR	9.4×10^{-5}	1.1×10^{-4}
FS-TR	4.4×10^{-4}	5.0×10^{-4}
PP	4.6×10^{-4}	5.0×10^{-4}
CSRZ	6.2×10^{-4}	6.4×10^{-4}

substantially larger than for the Gaussian bunch. However, as shown in the analysis for the Gaussian bunch, it is the curvature of the wake that actually affects the spectrum. The wake given by the CSRZ model seems to have the largest curvature along the bunch. The wakes given by FS-TR and PP models can be approximated by the linear chirp of opposite signs for a large part of the bunch. Therefore, we expect the bunching spectrum to be the broadest for the CSRZ model and the spectra for FS-TR and PP models to be similar to each other but shifted to the opposite sides. We also note that the sign of the CSR-induced chirp is crucial for implementing the compensation techniques using the seed laser chirp and/or wavelength shift.

The bunching spectra for rectangular bunch for different CSR models are shown in Fig. 17 and the rms bandwidths are given in Table IV. We see that our predictions based on the analysis of CSR wakes in Fig. 16 are in agreement with the calculated bandwidths. When we compare the bandwidths for Gaussian and rectangular bunches, we see that while the bandwidth is generally larger for a rectangular bunch, the CSR-induced part of the bandwidth is smaller. This can be explained by generally smaller curvature of the CSR wakes for the rectangular bunch.

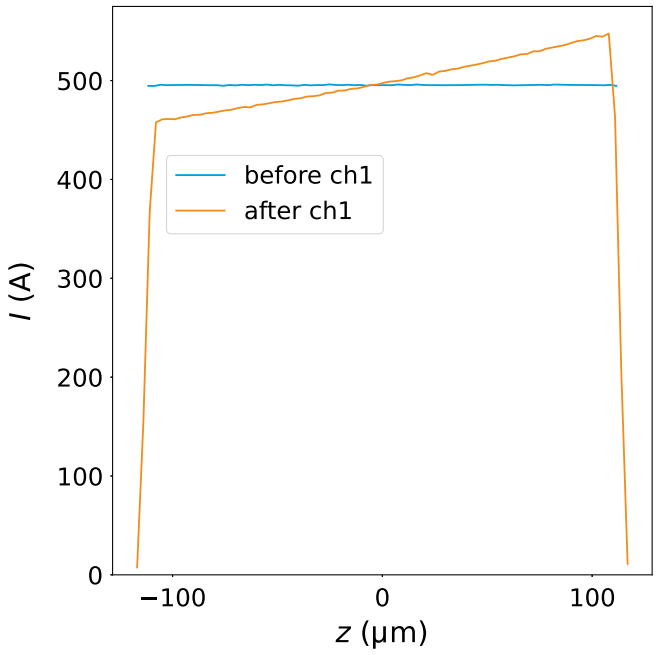

FIG. 18. The current profile of the rectangular electron bunch with $h_2 = 1.7 \times 10^{-7}$ before and after the first EEHG chicane.

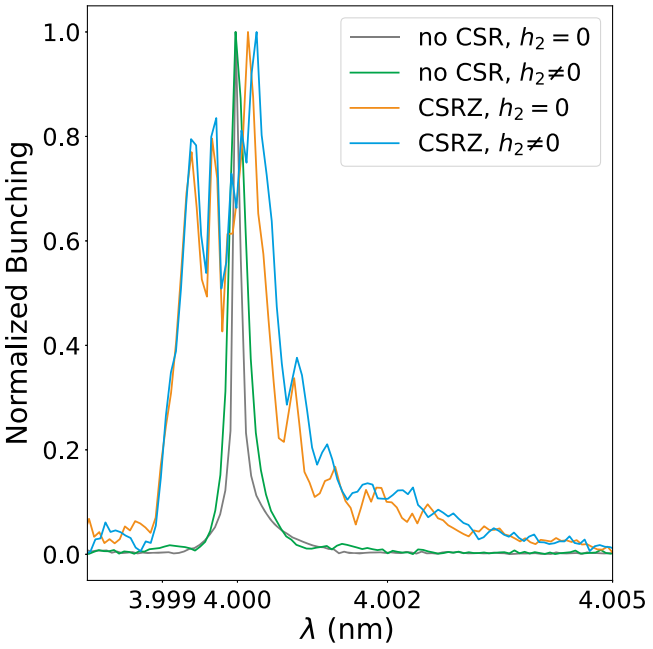

FIG. 19. Normalized bunching spectra with and without quadratic electron beam energy chirp and CSR wake given by CSRZ model for the rectangular bunch. If not equal to 0, $h_2 = 1.7 \times 10^{-7}$.

In the rectangular bunch case, it is also interesting to investigate the effect of quadratic electron beam energy chirp on the CSR-induced dynamics. As a test case, we assume the quadratic chirp of 7 MeV/ps^2 ($h_2 = 1.7 \times 10^{-7}$ if we follow the notation of [51]) reported for FERMI in [52]. Since the change in CSR originates from the change of the bunch shape, in Fig. 18, we show the current profile change due to the quadratic chirp after ch1.

The effect of quadratic electron beam energy chirp on the bunching spectrum is explained and calculated for Gaussian electron distribution in [51]. Based on this work, we expect a slight broadening of the bunching spectrum in our case, which can be seen in Fig. 19. The rms width of the spectrum is increased due to quadratic chirp by ≈20% in the absence of CSR. When CSR is included in the simulation, its contribution to the bandwidth is dominant and changes only by ≈4% with the quadratic energy chirp of the electron beam taken into account. This can be attributed to the fact that the change in the bunch shape illustrated in Fig. 18 is less significant than the linear chirp case.

V. CONCLUSION AND OUTLOOK

To summarize, CSR models broadly fall into three categories: time-domain models, frequency-domain models, and hybrid or multidimensional approaches. Time-domain models, such as those introduced by Saldin *et al.*

[11] and extended by Talman *et al.* [27], excel at predicting emittance growth and transient wakefield effects. The simplicity and emphasis of such approaches on spatial dynamics make them ideal for understanding CSR-induced beam degradation in linac and have been essential in accelerator design. However, they often lack the resolution required to study spectral effects, such as bandwidth broadening, which presents a weakness, especially in the case of seeded FELs. In contrast, frequency-domain models, including the approach utilized in this study [21,24], are computationally efficient in analyzing CSR impedance and shielding effects, making them particularly well suited for spectral studies. While the reliance on frequency domain models on 1D approximations could limit their accuracy when applied to complex beam and beamline geometries, results from these models can be benchmarked against experimental data to determine if additional perturbation is practical. The final category, hybrid or multidimensional approaches, such as those reported in Refs. [17,28], highlights the cumulative impact of CSR in complex systems. While computationally expensive, these methods offer the potential for the most accurate predictions. This method has the advantage that it can be combined with one of the other two categories, further adapted to reduce noise and leverage advanced techniques, i.e., machine learning and physics-informed artificial intelligence. Therefore, it represents a promising path toward more robust, efficient, and accurate CSR modeling.

In the work reported here, we have focused on comparing various formulations and their implications for practical accelerator systems to assess the importance of boundary conditions and transient effects, with the broader and more ambitious goal of advancing future multistage and 3D studies for the EEHG scheme. We have summarized the formulations of various models to calculate CSR within a chicane and reviewed the effect of the wakes on the efficiency of EEHG. We demonstrate that the instantaneous CSR impedance approach has certain advantages over the popular 1D CSR models, particularly when the bunch length is not sufficiently short, making chamber shielding crucial.

As a case study, we applied a few 1D CSR models to the 4 nm EEHG chicane configuration at FLASH. We have explored the consequential differences in CSR wakes and how these variances are manifested within the EEHG spectrum. Our results reveal that CSR-induced energy modulation has a more pronounced influence on EEHG performance in scenarios where the electron beam exhibits a strong linear energy chirp. This intensified effect is attributable to beam compression within the first chicane, amplifying CSR wakes upon chicane exit. Accurate consideration of CSR within the chicane is crucial for optimizing EEHG, as it substantially affects bunching and bandwidth. Then we extended the study to consider substantially different electron beam parameters, which are also typical for the EEHG scheme but in normal-conducting machines. We demonstrated that the CSR-induced bandwidth is generally smaller for flat current profile compared to Gaussian. We also estimated the effect of nominal quadratic electron beam energy chirp on the CSR-induced bandwidth to be on the order of a few percent.

The findings presented in this paper serve as a necessary foundation for future work. Specifically, we will investigate space charge effects and their impact on practical beam distributions in start-to-end simulations. Such multistage study will involve accounting for CSR influences as the beam traverses the linac and seeding section chicanes. It will also explore mitigation strategies, such as adjustments to the chirp—potentially nonlinear rather than the linear chirp considered in this study for FLASH—and optimizations of seed laser parameters, including pulse length, group delay dispersion, and third-order dispersion. More generally, the results of this paper expand on the quantitative foundation relevant to controlling properties of seeded FEL schemes by understanding and incorporating chamber-induced CSR effects. With the growing number of FEL facilities implementing seeded schemes—such as PSI, FERMI, and upcoming projects at SXFEL in China and FLASH in Germany—our findings offer valuable insights for optimizing chicane layouts and electron bunch properties.

Finally, if discrepancies emerge between the start-to-end simulations and the upcoming experimental campaigns, in that case, the instantaneous impedance approach discussed here for studying 1D CSR effects can be extended to explore 2D and 3D CSR effects for energy-chirped beams or adapted to investigate CSR dynamics within nonrectangular 3D boundary conditions, providing a broader perspective on CSR behavior in complex geometries.

ACKNOWLEDGMENTS

We express our gratitude to E. Ferrari, M. Pop, F. Pannek, and L. Schaper for their contribution to modeling and optimizing EEHG simulations. The author D. Z. thanks G. Stupakov for engaging discussions on various aspects of CSR theories. Furthermore, we deeply appreciate the support and guidance provided by S. Schreiber and the diverse team of FLASH2020+ project at DESY. This work has been supported by BMBF within the project 05K19GUC. The authors gratefully acknowledge the Gauss Centre for Supercomputing e.V. [53] for funding this project by providing computing time through the John von Neumann Institute for Computing (NIC) on the GCS Supercomputer JUWELS [54] at Jülich Supercomputing Centre (JSC) and Maxwell computational resources at Deutsches Elektronen-Synchrotron DESY, Hamburg, Germany.

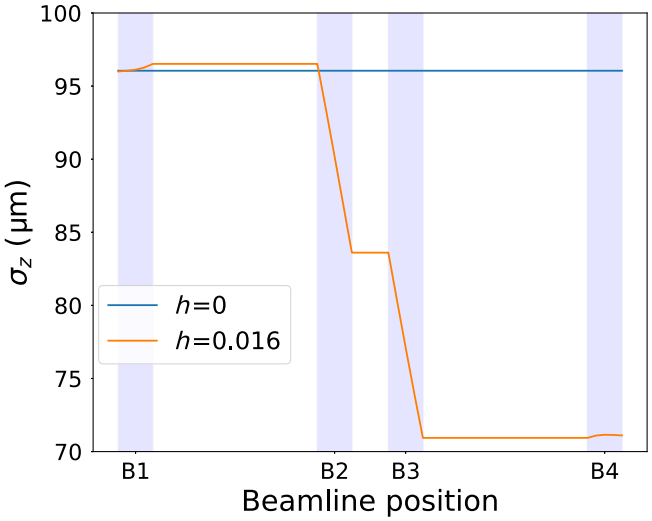

FIG. 20. Bunch length evolution inside ch1 for the nonchirped beam and the beam with nominal chirp value.

APPENDIX A: SUFFICIENT NUMBER OF SLICES

The bunch compression inside ch1 is illustrated in Fig. 20.

In order to verify that slicing each dipole in four parts is sufficient for the nominal chirp value of 15 MeV/ps, we compare resulting CSR wakes at the exit of the chicane for slicing into different number of sections N: (i) the impedance is lumped to the exit of the chicane ($N = 1$); (ii) the chicane is sliced into $N = 4$ sections with impedance lumped to the end of the drifts; (iii) four dipoles are sliced into four sections and four drifts ($N = 20$). The total wake at the exit of the chicane can be then calculated as

$$\Delta W_{\parallel}(z) = \sum_{j=1}^{N} \Delta W_{\parallel}^{(j)}(z^{(j)}) = q \sum_{j=1}^{N} \int_{-\infty}^{\infty} \Delta Z_{\parallel}^{(j)}(k) \exp\left(-\frac{k^2 \sigma_z^{(j)2}}{2}\right) e^{ikz^{(j)}} dk, \tag{A1}$$

where $\sigma_z^{(j)}$ is the Gaussian width of the electron bunch at the entrance of section j and $z^{(j)} = z\frac{\sigma_z^{(j)}}{\sigma_z^{(N)}}$ ensuring that the wake contributions from different slices along the bunch are properly tracked.

Comparing $N = 1$ to the sliced cases in Fig. 21, we see that the compression in the chicane changes the wakes significantly. At the same time, we see that $N = 20$ slicing is more than enough to capture the effect.

APPENDIX B: Δp_2 AT THE EXIT OF CH1

Figure 22 shows the modulation at the exit of the chicane. One can see that the overtaking fields are very close for both models, while the trailing fields and the energy loss by the central part of the bunch are gaining difference as the beam travels through the chicane. It is important to note that for CSRZ calculation, we assume an infinite drift at the exit of the chicane.

APPENDIX C: EFFECT OF LINEAR CHIRP ON THE BUNCHING SPECTRUM

As explained in [37] for a chirped electron beam, the target bunching harmonic will be shifted to

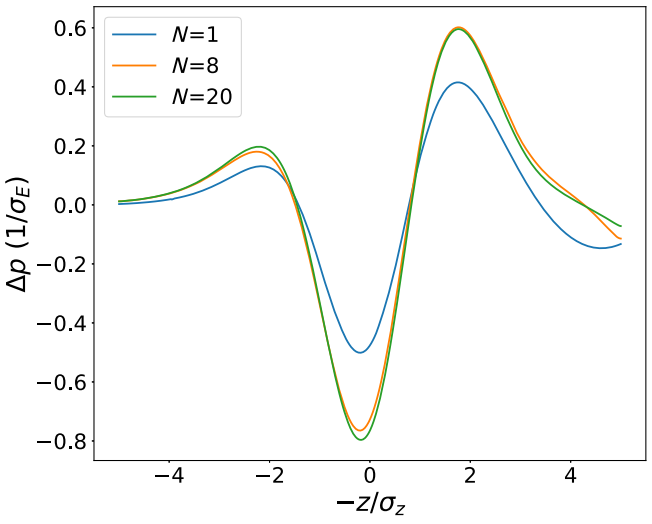

FIG. 21. CSR wakes at the exit of ch1 for different slicing.

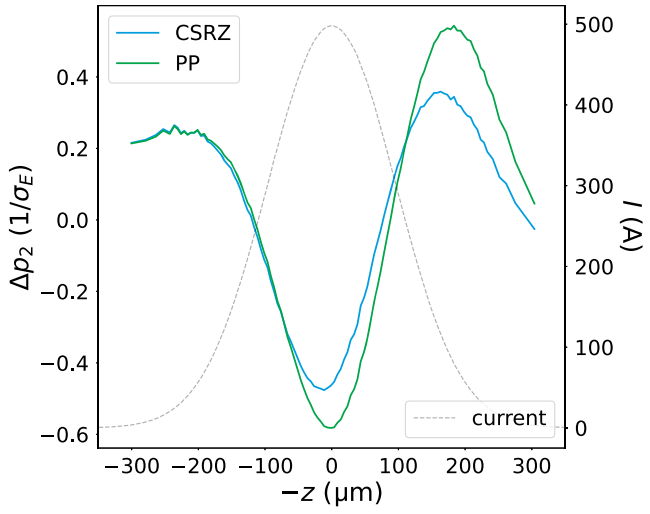

FIG. 22. Energy centroid at the exit of the chicane. Bunch current profile is given in gray. The bunch head is on the left.

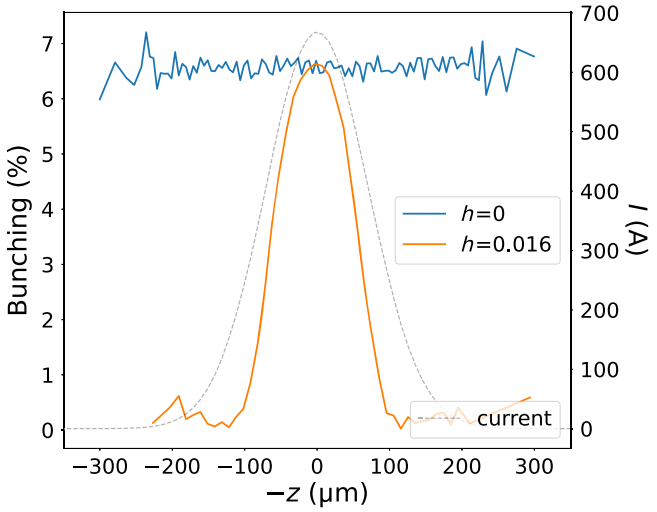

FIG. 23. Bunching profile for nonchirped and nominally chirped cases. The bunch current profile is given in gray. The chirped case results in the same bunching amplitude in the middle but has a considerably sharp envelope compared to nonchirped case.

$$a_E = \frac{mk_2/k_1(1+hB_1)-1}{1+hB}, \tag{C1}$$

where $h = \frac{dp}{dz}\frac{1}{k_1}$ is the electron beam energy chirp. In our case with $h = 0.016$ (equivalent to 15 MeV/ps), this corresponds to a wavelength shift of $+6.5\times10^{-4}$ nm. The bunching amplitude at the shifted harmonic can be optimized by slightly adjusting $R_{56}^{(2)}$ with respect to the original working point. As explained in [51], the linear chirp also contributes to the bandwidth. The contribution is partly due to the compression of the bunch in ch1. Most of the contribution, however, is due to the variation of $A_{1,2}$, $B_{1,2}$, and ξ_E along the bunch caused by the linear energy chirp. This results in a nonuniform bunching profile, as compared to the original nonchirped case, as shown in Fig. 23.

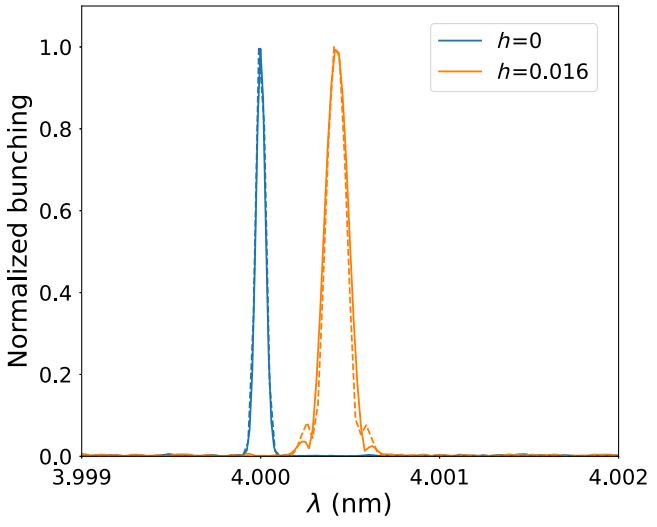

FIG. 24. Normalized bunching spectra for different values of linear chirp obtained from particle tracking (solid lines) and analytical formula (dashed lines).

In order to compare the spectral properties of the chirped and unchirped cases we calculate normalized bunching spectra for both. This is necessary since in the chirped case, the bunching is concentrated in ≈100 μm long part of the bunch and the bunching amplitude is averaged down by the tails of the bunch with vanishing bunching. The normalized spectra are given in Fig. 24.

In Fig. 24, we see the wavelength shift of $\approx +4.3\times10^{-4}$ nm. Next, we see that the peak naturally becomes significantly broader which we attribute to the reduced effective length of the bunch. We also clearly observe sidebands in the spectrum for the chirped case, separated from the target harmonic by 1.8×10^{-4} nm. Assuming those are typical sum- and difference-frequency sidebands, we estimate the wavelength of the interfering density modulation to be ≈90 μm. This corresponds well to the macroshape of the bunching profile in Fig. 23. A similar effect can be observed in the analytical treatment of the bunching spectrum given by equation (4) from [44] if we use semiempirical expressions for $A_1(z)$ and $A_2(z)$ from simulations.

APPENDIX D: COMPARISON OF THE EFFECT OF BUNCHING AND EMITTANCE ON SASE OR SEEDED FEL PERFORMANCE

The $\rho_{\rm fel} = \frac{1}{4\pi\gamma}[2\pi^2\sum_b (f_b(\xi)\lambda_u K_u)^2 (I_{\rm peak}/I_A)]^{1/3}$ parameter and $L_g = \lambda_u/4\pi\sqrt{3}\rho_{\rm fel}$ govern power growth along the radiator, as described in [46,47]. Here, γ is the beam energy factor, $I_{\rm peak}$ is the peak current, λ_u is the undulator period, and $f_b(\xi)$ is the kinematic coupling factor. The Ming Xie approximation [46] is a widely used semianalytical model for FEL performance, incorporating emittance,

TABLE V SASE and seeded parameter ranges (planar undulator/radiator case). CSR is neglected in the SASE case, and included in the seeded case as discussed.

	Radiation mode	
Parameters	SASE	Seeded
Radiation wavelength (nm)	4.0	4.0
E-beam energy (GeV)	1.35	1.35
E-beam chirp (MeV/ps)	25	6–14
E-beam energy spread (keV)	300	354–750
E-beam bunching factor	≈0.0001	0.07–0.014
E-beam peak current (A)	1000	500–610
E-beam emittance ϵ_n (mm mrad)	0.6–2.0	0.6–1.0
E-beam size σ_x/σ_y (μm)	45	45
E-beam average β (m)	5–10	8–10
Undulators period (m)	0.033	0.033
Undulators a_w parameter (variable gap)	0.831873	0.831873

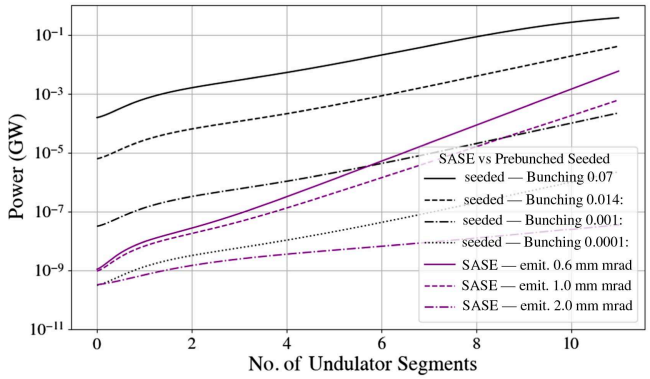

FIG. 25. Power (3D) growth along planar undulators at a 4 nm working point. The black lines (solid, dashed, and dotted) represent prebunched seeded FEL configurations with varying bunching factors for an idealized beam: emittance of 1.0 mm mrad, an average beta of ∼8 m, energy spread of 354 keV, and a current of 500 A. The relationship between the initial power due to prebunching and the final FEL power is evident. The purple lines (solid and dashed) correspond to SASE configurations with varying normalized emittances using SASE parameters from the table, highlighting the impact of emittance on reaching the exponential regime. Note that an average beta of 10 m corresponds to the lowest emittance, and 5 m corresponds to the largest emittance. Additionally, the seeded curve with a bunching factor of 0.0001 and the SASE curve with an emittance of 1.0 mm mrad illustrate the effect of an energy spread of ∼50 keV on the power growth curve.

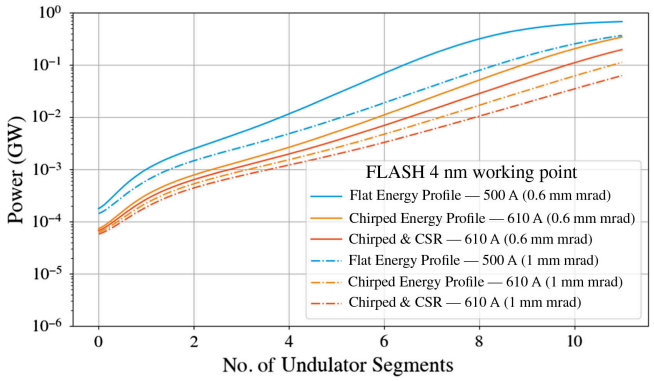

FIG. 26. 3D power growth along the planar undulator for the FLASH 4 nm working point as discussed in the paper. This plot highlights the impact of chirp and CSR-induced effects such as peak current, energy spread, and bunching for two different emittances. Solid lines correspond to an emittance of 0.6 mm mrad, while dash-dotted lines correspond to 1.0 mm mrad. The blue lines represent ideal configurations. The orange and red lines show the chirp effect with and without CSR from the simulation data with Gaussian profiles, respectively.

energy spread, focusing, and undulator parameters like period length and gap. The beam power is $P_{\text{beam}} = m_0 c^2 \gamma I_{\text{peak}}/e_0$, and the final power is $P_{\text{F}} = 1.6\rho_{\text{fel}} P_{\text{beam}}$ for SASE FELs. However, it does not account for the initial power of seeded prebunched beams. The modified formalism in Ref. [47] includes prebunched power in seeded schemes. In seeded prebunched beams, significant density modulation at the resonant wavelength exists before the radiator. Once the power surpasses the threshold $P_{\text{th}} = \rho_{\text{fel}}|b_1|^2 P_{\text{beam}}$, growth transitions from the quadratic regime to exponential, eventually reaching $P_{\text{F}}^* = P_{\text{F}} - P_{\text{th}}$. The Ming Xie gain curve for such beams is

$$P(z) = P_{\text{th}}\left[\frac{1}{3}\left(\frac{z}{L_{\text{g}}}\right)^2 \frac{1}{1+\frac{1}{3}(\frac{z}{L_{\text{g}}})^2+\frac{1}{2}\exp(\frac{z}{L_{\text{g}}}-\sqrt{3})} + \frac{1}{1+\frac{P_{\text{th}}}{P_{\text{F}}^*}\exp(\frac{z}{L_{\text{g}}}-\sqrt{3})}\right]. \tag{D1}$$

The full derivation of this formalism can be found in [47,48]. Here, we use Eq. (D1) alongside the parameters listed in Table V to highlight how the studies in this paper contribute to optimizing FEL performance.

The bunching factor, which quantifies the density modulation of the electron beam at a given harmonic, plays an essential role in the initial FEL gain. Chirp-induced effects, especially when considering CSR, degrade beam parameters such as bunching, reduce radiative interaction efficiency, increase gain length L_g, and lead to slower power growth. As shown in Ref. [55], undesired dispersion effects can be mitigated by introducing a chirp profile to the laser pulse. However, only one optimal group delay dispersion (GDD) value can flatten the phase of FEL radiation and lead to a Fourier-limited FEL pulse.

This makes characterizing CSR, as presented in this paper, essential for estimating the maximum GDD needed for the laser pulse and for performing start-to-end simulations to evaluate the efficiency and stability of the machine at optimal working points. While a detailed discussion of this approach is outside the scope of this paper, we demonstrate the impact of reduced bunching in seeded FELs and compare it with the effects of emittance and energy spread in SASE FELs in Fig. 25.

Additionally, we show the effect of reduced bunching and degraded beam parameters for the 4 nm working point of FLASH using a Gaussian profile, as illustrated in Fig. 26. The seeded parameters in Table II are used. For the chirped energy profile, the peak current and energy spread increase from 500 A and 354 keV to 610 A and 680 keV, while the bunching is reduced from 6% to approximately 4%. In the presence of CSR, the energy spread is further increased to 750 keV. Configurations with low emittance (0.6 mm mrad) achieve higher power growth, while larger emittance (1.0 mm mrad) delays the transition to the exponential regime, as shown for both seeded and SASE scenarios. Setup and beam parameters that ensure saturation of the EEHG signal are essential for maximizing harmonic generation efficiency and preserving the advantages of seeded FEL operation, such as near-Fourier-limited

pulses and minimal spectral broadening. CSR-induced changes to beam parameters, including energy spread and peak current, significantly contribute to the observed reduction in FEL power growth in the studied configurations.

[1] Y. S. Derbenev, J. Rossbach, E. L. Saldin, and V. D. Shiltsev, Microbunch radiative tail-head interaction, DESY, Hamburg, Technical Report No. TESLA-FEL-95-05, 1995, https://cds.cern.ch/record/291102.

[2] S. D. Mitri *et al.*, Design and simulation challenges for FERMI@elettra, Nucl. Instrum. Methods Phys. Res., Sect. A **608**, 19 (2009).

[3] S. Heifets and G. Stupakov, Beam instability and microbunching due to CSR, in *Proceedings of the 2001 Particle Accelerator Conference (PAC), Chicago* (2001), https://accelconf.web.cern.ch/p01/PAPERS/TPPH081.PDF.

[4] M. Borland, Y. Chae, P. Emma, J. Lewellen, V. Bharadwaj, W. Fawley, P. Krejcik, C. Limborg, S. Milton, H.-D. Nuhn, R. Soliday, and M. Woodley, Start-to-end simulation of self-amplified spontaneous emission free electron lasers from the gun through the undulator, Nucl. Instrum. Methods Phys. Res., Sect. A **483**, 268 (2002).

[5] L. H. Yu, Generation of intense UV radiation by subharmonically seeded single-pass free-electron lasers, Phys. Rev. A **44**, 5178 (1991).

[6] G. Stupakov, Using the beam-echo effect for generation of short-wavelength radiation, Phys. Rev. Lett. **102**, 074801 (2009).

[7] E. Hemsing, G. Marcus, W. M. Fawley, R. W. Schoenlein, R. Coffee, G. Dakovski, J. Hastings, Z. Huang, D. Ratner, T. Raubenheimer, and G. Penn, Soft x-ray seeding studies for the SLAC Linac Coherent Light Source II, Phys. Rev. Accel. Beams **22**, 110701 (2019).

[8] M. Pop, F. Curbis, S. Werin, and E. Allaria, Mitigation of CSR induced spectral broadening in EEHG FEL, Nucl. Instrum. Methods Phys. Res., Sect. A **1048**, 167926 (2023).

[9] D. Samoilenko, F. Curbis, W. Hillert, P. Niknejadi, F. Pannek, G. Paraskaki, M. Pop, and S. Werin, Discussion on CSR instability in EEHG simulation, in *Proceedings of the 12th International Particle Accelerator Conference, Campinas, SP, Brazil* (JACoW, Geneva, Switzerland, 2021), 10.18429/JACoW-IPAC2021-TUPAB103.

[10] D. Samoilenko, W. Hillert, F. Pannek, S. Ackermann, E. Ferrari, N. Mirian, P. Niknejadi, G. Paraskaki, L. Schaper, F. Curbis, M. Pop, and S. Werin, Sensitivity of EEHG simulations to dynamic beam parameters, in *Proceedings of the 13th International Particle Accelerator Conference (IPAC'22), Bangkok, Thailand* (IOP Publishing, United Kingdom, 2023), 10.1088/1742-6596/2420/1/012024.

[11] E. L. Saldin, E. A. Schneidmiller, and M. V. Yurkov, On the coherent radiation of an electron bunch moving in an arc of a circle, Nucl. Instrum. Methods Phys. Res., Sect. A **398**, 373 (1997).

[12] G. Stupakov and I. Kotelnikov, Calculation of coherent synchrotron radiation impedance using the mode expansion method, Phys. Rev. ST Accel. Beams **12**, 104401 (2009).

[13] M. D. Dohlus and T. L. Limberg, CSRtrack: Faster calculation of 3-D CSR effects, in *Proceedings of the International Free Electron Laser Conference (FEL'04), Trieste, Italy* (JACoW, Geneva, Switzerland, 2004).

[14] C. Mayes and G. Hoffstaetter, Exact 1D model for coherent synchrotron radiation with shielding and bunch compression, Phys. Rev. ST Accel. Beams **12**, 024401 (2009).

[15] J. Esberg, R. Apsimon, A. Latina, and D. Schulte, Effect of CSR shielding in the compact linear collider, in *Proceedings of the 5th International Particle Accelerator Conference (IPAC'14), Dresden, Germany* (JACoW, Geneva, Switzerland, 2014), pp. 1337–1339, 10.18429/JACoW-IPAC2014-TUPME003.

[16] D. Sagan, G. Hoffstaetter, C. Mayes, and U. Sae-Ueng, Extended one-dimensional method for coherent synchrotron radiation including shielding, Phys. Rev. ST Accel. Beams **12**, 040703 (2009).

[17] W. Lou and G. Hoffstaetter, Coherent synchrotron radiation wake expressions with two bending magnets and simulation results for a multiturn energy-recovery linac, Phys. Rev. Accel. Beams **23**, 054404 (2020).

[18] G. Stupakov and I. Kotelnikov, Shielding and synchrotron radiation in toroidal waveguide, Phys. Rev. ST Accel. Beams **6**, 034401 (2003).

[19] T. Agoh and K. Yokoya, Calculation of coherent synchrotron radiation using mesh, Phys. Rev. ST Accel. Beams **7**, 054403 (2004).

[20] T. Agoh, Steady fields of coherent synchrotron radiation in a rectangular pipe, Phys. Rev. ST Accel. Beams **12**, 094402 (2009).

[21] D. Zhou, Coherent synchrotron radiation and microwave instability in electron storage rings, Ph.D. thesis, The Graduate University for Advanced Studies, 2011.

[22] T. Agoh, Transient fields of coherent synchrotron radiation in a rectangular pipe, arXiv:2306.15894.

[23] D. Zhou, An alternative 1D model for CSR with chamber shielding, in *Proceedings of the International Particle Accelerator Conference (IPAC'12), New Orleans, Louisiana* (JACoW, Geneva, Switzerland, 2012), pp. 52–54, https://jacow.org/IPAC2012/papers/MOOBB03.pdf.

[24] D. Zhou, K. Ohmi, K. Oide, L. Zang, and G. Stupakov, Calculation of coherent synchrotron radiation impedance for a beam moving in a curved trajectory, Jpn. J. Appl. Phys. **51**, 016401 (2011).

[25] A. Brynes *et al.*, Understanding 1D to 3D coherent synchrotron radiation effects, in *Proceedings of the 39th Free Electron Laser Conference (FEL'19), Hamburg, Germany* (JACoW, Geneva, Switzerland, 2019), pp. 578–583.

[26] K. L. F. Bane, F.-J. Decker, Y. Ding, D. Dowell, P. Emma, J. Frisch, Z. Huang, R. Iverson, C. Limborg-Deprey, H. Loos, H.-D. Nuhn, D. Ratner, G. Stupakov, J. Turner, J. Welch, and J. Wu, Measurements and modeling of coherent synchrotron radiation and its impact on the linac coherent light source electron beam, Phys. Rev. ST Accel. Beams **12**, 030704 (2009).

[27] R. Talman, N. Malitsky, and F. Stulle, Emittance growth due to static and radiative space charge forces in an electron bunch compressor, Phys. Rev. ST Accel. Beams **12**, 014201 (2009).

[28] A. Brynes, P. Smorenburg, I. Akkermans, E. Allaria, L. Badano, S. Brussaard, M. Danailov, A. Demidovich, G. De Ninno, D. Gauthier *et al.*, Beyond the limits of 1D coherent synchrotron radiation, New J. Phys. **20**, 073035 (2018).

[29] C. Mayes, Computational approaches to coherent synchrotron radiation in two and three dimensions, J. Instrum. **16**, P10010 (2021).

[30] J. Rossbach, J. R. Schneider, and W. Wurth, 10 years of pioneering X-ray science at the Free-Electron Laser FLASH at DESY, Phys. Rep. **808**, 1 (2019).

[31] ELEGANT: A flexible SDDS-compliant code for accelerator simulation (2000), 10.2172/761286.

[32] A. Faltens and L. J. Laslett, Longitudinal coupling impedance of a stationary electron ring in a cylindrical geometry, Part. Accel. **4**, 151 (1973), https://cds.cern.ch/record/1107915.

[33] S. Heifets, G. Stupakov, and S. Krinsky, Coherent synchrotron radiation instability in a bunch compressor, Phys. Rev. ST Accel. Beams **5**, 064401 (2002).

[34] M. Borland, Simple method for particle tracking with coherent synchrotron radiation, Phys. Rev. ST Accel. Beams **4**, 070701 (2001).

[35] M. Borland, User's manual for elegant, https://ops.aps.anl.gov/manuals/elegant_latest/elegant.pdf.

[36] G. Stupakov and P. Emma, CSR wake for a short magnet in ultrarelativistic limit, SLAC Report No. SLAC-PUB-9242, 2002, https://cds.cern.ch/record/580930.

[37] Z. Huang, D. Ratner, G. Stupakov, and D. Xiang, Effects of energy chirp on echo-enabled harmonic generation free-electron lasers, Technical Report No. SLAC-PUB-13547, 948487, 2009, 10.2172/948487.

[38] Y. Cai, Two-dimensional theory of coherent synchrotron radiation with transient effects, Phys. Rev. Accel. Beams **24**, 064402 (2021).

[39] R. Warnock and M. Venturini, Evolving bunch and retardation in the impedance formalism, in *Proceedings of the 2003 Particle Accelerator Conference, Portland, OR* (IEEE, New York, 2003), Vol. 5, pp. 3144–3146.

[40] K. Oide, T. Abe, K. Akai, Y. Funakoshi, T. Kageyama, H. Koiso, K. Ohmi, Y. Ohnishi, K. Shibata, Y. Suetsugu *et al.*, A few issues on the upgrade of KEKB B–factory, in *Proceedings of the 23rd 2009 Particle Accelerator Conference, Vancouver, Canada* (2009), p. 23, https://accelconf.web.cern.ch/pac2009/papers/mo3rai01.pdf.

[41] L. Wang, H. Ikeda, K. Ohmi, K. Oide, and D. Zhou, Validation of the microwave instability in the damping ring of SuperKEKB using VFP solver, in *Proceedings of the International Particle Accelerator Conference (IPAC'13), Shanghai, China* (JACoW, Geneva, Switzerland, 2013), pp. 1604–1606, https://jacow.org/IPAC2013/papers/TUPME017.pdf.

[42] B. Billinghurst, J. Bergstrom, C. Baribeau, T. Batten, L. Dallin, T. May, J. Vogt, W. Wurtz, R. Warnock, D. Bizzozero *et al.*, Observation of wakefields and resonances in coherent synchrotron radiation, Phys. Rev. Lett. **114**, 204801 (2015).

[43] E. Hemsing, Bunching phase and constraints on echo enabled harmonic generation, Phys. Rev. Accel. Beams **21**, 050702 (2018).

[44] N. S. Mirian, G. Perosa, E. Hemsing, E. Allaria, L. Badano, P. Cinquegrana, M. B. Danailov, G. De Ninno, L. Giannessi, G. Penco, S. Spampinati, C. Spezzani, E. Roussel, P. R. Ribič, M. Trovó, M. Veronese, and S. Di Mitri, Characterization of soft x-ray echo-enabled harmonic generation free-electron laser pulses in the presence of incoherent electron beam energy modulations, Phys. Rev. Accel. Beams **24**, 080702 (2021).

[45] M. Beye and S. Klumpp, *FLASH2020+—upgrade of FLASH: Conceptual design report* (Verlag Deutsches Elektronen-Synchrotron, Hamburg, 2020), pp. 1 online resource (iii, 115 pages): illustrations, diagrams, 10.3204/PUBDB-2020-00465.

[46] M. Xie, Design optimization for an x-ray free electron laser driven by SLAC linac, in *Proceedings of the Particle Acceerator Conferemce (PAC'95), Dallas, TX* (JACoW, Geneva, Switzerland, 1995), pp. 183–185, https://jacow.org/p95/ARTICLES/TPG/TPG10.pdf.

[47] L. Giannessi, Seeding and harmonic generation in free-electron lasers, in *Synchrotron Light Sources and Free-Electron Lasers* (Springer, Cham, 2016), pp. 195–223, 10.1007/978-3-319-14394-1_3.

[48] P. Niknejadi, D. Samoilenko, F. Pannek, G. Paraskaki, H. Wenzel, J. Zemella, L. Schaper, M. Asatrian, M. Vogt, P. Amstutz, S. Schreiber, S. Ackermann, T. Lang, W. Hillert, and E. Ferrari, Optimization and characterization of externally seeded FLASH1, in *Proceedings of the 41st International Free Electron Laser Conference (FEL'24), Warsaw, Poland* (JACoW, Geneva, Switzerland, 2024), https://fel2024.org.

[49] R. L. Warnock, Coherent synchrotron radiation in whispering gallery modes: Theory and evidence, arXiv:1708.05500.

[50] D. Bizzozero, E. Gjonaj, and H. De Gersem, Modeling coherent synchrotron radiation with a discontinuous Galerkin time-domain method, J. Comput. Phys. **394**, 745 (2019).

[51] E. Hemsing, B. Garcia, Z. Huang, T. Raubenheimer, and D. Xiang, Sensitivity of echo enabled harmonic generation to sinusoidal electron beam energy structure, Phys. Rev. Accel. Beams **20**, 060702 (2017).

[52] B. Mahieu, E. Allaria, D. Castronovo, M. B. Danailov, A. Demidovich, G. D. Ninno, S. D. Mitri, W. M. Fawley, E. Ferrari, L. Fröhlich, D. Gauthier, L. Giannessi, N. Mahne, G. Penco, L. Raimondi, S. Spampinati, C. Spezzani, C. Svetina, M. Trovò, and M. Zangrando, Two-colour generation in a chirped seeded free-electron laser: A close look, Opt. Express **21**, 22728 (2013).

[53] www.gauss-centre.eu

[54] Jülich Supercomputing Centre, JUWELS cluster and booster: Exascale pathfinder with modular supercomputing architecture at Juelich Supercomputing Centre, J. Large-Scale Res. Facil. **7**, A183 (2021).

[55] D. Gauthier, P. Rebernik Ribič, G. De Ninno, E. Allaria, P. Cinquegrana, M. B. Danailov, A. Demidovich, E. Ferrari, L. Giannessi, B. Mahieu, and G. Penco, Spectrotemporal shaping of seeded free-electron laser pulses, Phys. Rev. Lett. **115**, 114801 (2015).